Revisiting Properties of Edge-Bridged Bromide Tantalum Clusters in the Solid-State, in Solution and vice-versa: An Intertwined Experimental and Modelling Approach

Maxence Wilmet, Clément Lebastard, Flavien Sciortino, Clothilde Zerbino, Luke Macaleese, Fabien Chirot, Philippe Dugourd, Fabien Grasset, Yoshitaka Matsushita, Tetsuo Uchikoshi, et al.

Received 00th January 20xx,
Accepted 00th January 20xx

DOI: 10.1039/x0xx00000x

Revisiting Properties of Edge-Bridged Bromide Tantalum Clusters in the Solid-State, in Solution and vice-versa: An Intertwined Experimental and Modelling Approach

Maxence Wilmet,[‡a,b,c] Clément Lebastard,[‡a] Flavien Sciortino,[d] Clothilde Comby-Zerbino,[e] Luke MacAleese,[e] Fabien Chirot,[f] Philippe Dugourd,[e] Fabien Grasset,[b,c] Yoshitaka Matsushita,[g] Tetsuo Uchikoshi,[c,g] Katsuhiko Ariga,[d,h] Pierric Lemoine,[b] Adèle Renaud,[b] Karine Costuas,[b]* Stéphane Cordier[b]*

Edge-bridged halide tantalum clusters based on the $\{Ta_6Br_{12}\}^{4+}$ core have been the topic of many physico-structural investigations both in solution and in the solid-state. Despite a large number of studies, the fundamental correlations between compositions, local symmetry, electronic structures of $[\{Ta_6Br^i_{12}\}L^a_6]^{m+/n-}$ cluster units (L = Br or H_2O, in solution and at the solid-state), redox states, and vibrational and absorption properties are still not well established. Using $K_4[\{Ta_6Br^i_{12}\}Br^a_6]$ as starting precursor (i: inner, a: apical), we have investigated the behavior of the $[\{Ta_6Br^i_{12}\}Br^a_6]^{4-}$ cluster unit in terms of oxidation properties and chemical modifications both in solution (water and organic solvent) and after recrystallization. A wide range of experimental techniques in combination with quantum chemical simulations afford new data that allow to reveal the puzzling behavior the cluster units in response to changes in their environment. Apical ligands undergo changes like modifications of interatomic distances to complete substitutions in solution that modify noticeably the cluster physical properties. Changes of oxidation state of the cluster units also occur, which modifies significantly their physical properties, including optical properties, which can thus be used as fingerprint. A subtle balance exists between the number of substituted apical ligands and the cluster oxidation state. This study provides new information about the exact nature of the species formed during the transition from solid-state to solutions and *vice-versa*. This shines new perspectives on optimization protocols for the design of Ta_6 cluster-based materials.

Introduction

Metal clusters are building blocks made of metal with precise nuclearity, size and shape. The geometry of the metal aggregates, the nature of metal atoms and that of their surrounding ligands drive the chemical and physical properties of the cluster units. Novel materials include such cluster units with the hope that they maintain their intrinsic physical properties in the bulk.[1] A dedicated chemical engineering has been developed to create metal-based cluster assemblies with specific tailored properties using solid-state chemistry as well as solution chemistry or combination of both.[2] In the field of materials chemistry, metal atom cluster building blocks are particularly useful for the elaboration of nanocomposites. A wide range of multifunctional cluster-based composite materials and surfaces are reported in the literature. Cluster-based composite materials are obtained by embedding clusters in organic or inorganic matrices. The role of the cluster is manifold. As an illustration, the cluster can be used to bring specific functionalities (luminescence, magnetism, redox properties for example) or acts as a cross linker to reinforce organic polymer matrices.[3, 4] Another structuration is to associate metal clusters via organic or inorganic linkers for the design of multi-

[a] Saint Gobain Research Paris, F-93300 Aubervilliers, France
[b] Univ Rennes, CNRS, ISCR (Institut des Sciences Chimiques de Rennes) – UMR 6226, F-35000 Rennes, France
[c] CNRS–Saint-Gobain–NIMS, UMI 3629, Laboratory for Innovative Key Materials and Structures (LINK), National Institute for Materials Science, 1-1 Namiki, 305-0044 Tsukuba, Japan
[d] WPI Center for Materials Nanoarchitectonics (MANA), National Institute for Materials Science (NIMS), 1-1 Namiki, Tsukuba, Ibaraki 305-0044, Japan
[e] Univ Lyon, Université Claude Bernard Lyon 1, CNRS, Institut Lumière Matière, F-69622, Lyon, France
[f] Univ Lyon, Université Claude Bernard Lyon 1, ENS de Lyon, Institut des Sciences Analytiques, UMR 5280, 5 rue de la Doua, F-69100 Villeurbanne, France.
[g] Research Center for Functional Materials, National Institute for Materials Science (NIMS), 1-1 Namiki, Tsukuba, Japan.
[h] v- Department of Advanced Materials Science, Graduate School of Frontier Sciences, The University of Tokyo, Kashiwa, Chiba 277-8561, Japan
‡ The first two authors contributed equally to the publication.

Supplementary Information (SI) available: Experimental procedures. Computational details. XRPD patterns. Le Bail and Rietveld refinement data. Thermal gravimetric analysis. Raman and UV-visible spectra. Optimized Cartesian coordinates. Simulated Raman spectra. TD-DFT excitations. **2$_\gamma$** XRPD cif file. See DOI: 10.1039/x0xx00000x

functional porous coordination compounds able to combine multiple functionalities synergistically for specific applications.[5] Among the large family of inorganic metal clusters, those exhibiting an octahedral metal core are certainty the most widely studied. They are mainly encountered for metal atoms of the fifth and sixth columns of the periodic table (M = Nb, Ta, Mo, W and Re) and are obtained by solid-state chemistry. In these systems, the metal M_6 core is stabilized by apical (a) and edge-bridged or face-capped inner (i) ligands to form $[M_6X^i_{12}X^a_6]$ and $[M_6Q^i_8X^a_6]$ units (Q = chalcogen and/or halogen; X = halogen). After their syntheses by solid-state chemistry at high temperature, most of those compounds are soluble in appropriate solvent and thus processable for the design of hybrid materials and coordination compounds (with or without exchange of apical ligands). Face-capped $[M_6Q^i_8X^a_6]$ cluster units (M = Mo, W and Re) have been particularly studied as integratable building blocks in composites or onto surfaces.[6-8] The edge-bridged $[M_6X^i_{12}X^a_6]$ cluster units (M = Nb and Ta) have received much less attention than their face-capped homologous in the literature. Nevertheless, their structure and chemical and physical properties were shown to be of interest for many applications: i) $[Ta_6Br^i_{12}(H_2O)^a_6]^{n+}$ units were used for phasing X-ray crystal structures in protein crystallography owing to their solubility in water and their high electronic density,[9] ii) $\{M_6X^i_{12}\}^{n+}$ edge-bridged metal cluster-cores were used as metal precursor for the *in-situ* synthesis of metal oxide as molecular size pillars in smectite clays,[10] iii) some $[M_6X^i_{12}L^a_6]$ units are catalyzing organic reactions,[11] iv) redox-active $[M_6X^i_{12}L^a_6]$ units were employed to fabricate modified electrodes (L = X or H_2O),[12] and v) $[Ta_6Br^i_{12}(H_2O)^a_6]^{2+}$@2-γCD inclusion complexes (CD = cyclodextrin) have been used to prepare self-assemblies of clusters and polyoxometalates, called CLUSPOM.[13] Recently, we have been investigating the use of $[Ta_6Br^i_{12}Br^a_6]^{n-}$ and $[Ta_6Br^i_{12}(H_2O)^a_6]^{m+}$ cluster units as ultra-violet (UV) and near-infrared (NIR) filters for energy saving applications: i) glass coater nanocomposites containing $[\{Ta_6Br^i_{12}\}Br^a_6]^{4-}$, with high transparency in the visible range , ii) ITO surfaces functionalized by $[\{Ta_6Br^i_{12}\}(H_2O)^a_6]^{2+}$ by the means of electrophoretic deposition for IR-blocking applications and iii) electrochromic cells based on $[\{Ta_6Br^i_{12}\}(H_2O)^a_6]^{2+}$.[14-16] For the latter, the control of the redox state of $[\{Ta_6Br^i_{12}\}(H_2O)^a_6]^{2+}$ by application of a variable electric potential allows the reversible tuning of the cells color from green to light yellow-brown.[14] The formation of $[\{Ta_6Br^i_{12}\}(H_2O)^a_6]^{2+}$ by simple dissolution of $K_4[\{Ta_6Br^i_{12}\}Br^a_6]$ in water can also be exploited to undergo further chemical modifications with the addition of halide salts of alkali or rare earth.[17]

Unfortunately, no comprehensive study exists to date which enable to understand and fully control the final chemical composition of these edge-bridged clusters. Following the work of Chabrié who is at the origin of the research dealing with reduced tantalum halides,[18] Chapin demonstrated that the dissolution in acidic water of the product issued from the reduction of $TaBr_5$ and $TaCl_5$ by sodium amalgam leads, respectively, to $Ta_6Br_{14}{\cdot}7H_2O$ and $Ta_6Cl_{14}{\cdot}7H_2O$.[19] The X-ray analyses of the powders resulting from solvent evaporation evidenced products with $Ta_6X_{14}{\cdot}7H_2O$ (X = Cl, Br) chemical composition. Later, Vaughan *et al.* evidenced the presence of a Ta_6 cluster surrounded by edge-bridging halogen ligands.[20] In solution, no heavy atoms like halogen was localized in apical position meaning that in solution the $\{Ta_6X^i_{12}\}^{2+}$ cluster core is stabilized only by water molecules to form a $[\{Ta_6Br^i_{12}\}(H_2O)^a_6]^{2+}$ cluster unit. Then, Burbank, using single crystal X-ray diffraction technique, has shown that the structure of $Ta_6Cl_{14}{\cdot}7H_2O$ is based on *trans*-$[\{Ta_6Cl^i_{12}\}Cl^a_2(H_2O)^a_4]$ cluster unit with a disordered orientation.[21] On the other hand, Spreckelmeyer,[22] Schäfer *et al.*,[23] Brnicevic *et al.*[24] and Koknat *et al.*[25] found compounds with formulation $Ta_6X_{14}{\cdot}8H_2O$. McCarley and collaborators suggested the possibility of several crystalline hydrated species containing $[\{Ta_6X^i_{12}\}X^a_2(H_2O)^a_4$ complexes.[26] It turns out that the water content per unit cell may be sensitive to the preparation methods. Sokolov *et al.*[17] and Brnicevic and collaborators[27] have shown that the dissolution of $Ta_6Br_{14}.7H_2O$ and $Ta_6Br_{14}.8H_2O$ leads to $[\{Ta_6Br^i_{12}\}(H_2O)^a_6]^{2+}$ cluster units that can be crystallized along with different types of cations and anions to form compounds like $[\{Ta_6Br^i_{12}\}(H_2O)^a_6][CuBr_2X_2]$, $[\{Ta_6Br^i_{12}\}(H_2O)^a_6](SO_4){\cdot}8.5H_2O$ or $Cs[\{Ta_6Br^i_{12}\}(H_2O)^a_6]Br_3{\cdot}6H_2O$. Indeed and as previously stressed by Hughes *et al.*,[28] crystallizations from aqueous solutions that contain $\{M_6X^i_{12}\}$-core clusters provides a wide range of hydrate derivatives with the general $[\{M_6X^i_{12}\}X_{6-n}(H_2O)_n]{\cdot}mH_2O$ formula. For n = 4, at least 3 compounds have been evidenced with m = 3, 4 and 5. The general formula of these derivatives can be written as $[\{M_6X^i_{12}\}X^a_2(H_2O)^a_4]{\cdot}xH_2O$ in which $[\{M_6X^i_{12}\}X^a_2(H_2O)^a_4]$ is formally neutral. It turns out that the number of crystallization water molecules (x) strongly impact the crystal structures of the hydrates as evidenced by important differences in the X-ray powder diffraction patterns and to a lesser extent in their Raman response as reported and discussed for the first time in the present work. The preparation methods, in particular the evaporation process (in air or using solvent evaporation techniques) is a key factor but no rationalization is available to date to allow a complete control.[22,29-32]

If the crystal chemistry and the chemistry of compounds resulting from the dissolution/crystallization of solid state $\{Ta_6Br^i_{12}\}$ based bromides in water has been intensively investigated, no comprehensive study is available to date. The step by step comprehensive investigation of the chemistry resulting from organic solvent dissolution/crystallization of solid state $\{Ta_6Br^i_{12}\}$ based bromides is also missing. Moreover, the fundamental correlations between compositions, local symmetry and electronic structures of $[\{Ta_6Br^i_{12}\}L^a_6]^{m+/n-}$ cluster units (L = Br or H_2O, in solution and at the solid-state) and their redox, vibrational and absorption properties are still not well established. However, this constitutes mandatory data toward the design of optimized edge-bridged cluster based materials and devices.

In this work, we have investigated the behaviour of the $[\{Ta_6Br^i_{12}\}Br^a_6]^{4-}$ cluster units using $K_4[\{Ta_6Br^i_{12}\}Br^a_6]$ as starting solid state precursor, in terms of oxidation properties and chemical composition in solution (water and organic solvents) and after recrystallization using a wide range of techniques: mass spectrometry, Raman and UV-visible spectroscopies, electrochemistry, X-ray diffraction investigations at different temperatures and quantum chemical simulations. This study combining experimental and theoretical studies brings new data which are the missing pieces of knowledge among dispersed data reported in the literature

on the $\{Ta_6Br^i_{12}\}^{m+}$ cluster core based species. This allows completing the puzzle of the full rationalization of the exact nature Ta_6-based cluster units when changing from solid-state to solutions and *vice-versa* to optimize the protocols for the design of Ta_6 cluster-based materials.

Results

Synthesis and characterization of 1, $2_{\alpha,\beta,\gamma}$ and 3 by X-ray diffraction, thermal gravimetric analyses (TGA) and Raman spectroscopy.

$K_4[\{Ta_6Br^i_{12}\}Br^a_6]$ was prepared using an optimized method derived from that of F.W. Koknat *et al.*[25] The synthesis consists in the solid-state reduction of $TaBr_5$ by an excess of tantalum metal in the presence of KBr as detailed in SI. After optimization, we found that the best reaction yield is obtained for the KBr:$TaBr_5$:Ta proportions of 4:(14/5):4 using a reaction temperature of 650°C for 24h. This as-prepared powder sample is named **1** thereafter in the text. To date, none of the research groups working in the domain reported crystallographic data about $K_4[\{Ta_6Br^i_{12}\}Br^a_6]$. The single structural analysis is that of Koknat *et al.*,[25] who reported that $K_4[\{Ta_6Br^i_{12}\}Br^a_6]$ is isostructural with the niobium homologous $K_4[\{Nb_6Br^i_{12}\}Br^a_6]$ "by visual comparison of X-ray powder patterns". In the present work, we report for the first time the unit cell parameters of $K_4[\{Ta_6Br^i_{12}\}Br^a_6]$ refined from X-ray powder diffraction data (Table 1). The analysis of the X-ray powder pattern of as prepared **1** (Fig. S1) revealed the presence of $K_4[\{Ta_6Br^i_{12}\}Br^a_6]$ as the main phase along with an excess of tantalum powder and KBr as secondary phases. Further analyses described in SI show the following proportion in **1**: 12.7 % Ta, 21.0 % KBr. The refinement of the X-ray diffraction pattern evidences that $K_4[Ta_6Br^i_{12}Br^a_6]$ crystallizes in the $K_4Nb_6Cl_{18}$-type structure (space group *C*2/*m*, No. 12) with the refined unit cell parameters: a = 10.46(1) Å, b = 17.19(2) Å, c = 9.99(1) Å, β = 114.89(1)°, and V = 1629.1(3) $Å^3$; Z = 2). In this type of structure, the $[M_6X^i_{12}X^a_6]^{4-}$ cluster unit is centered on a 2*a* Wyckoff position implying the C_{2h} local symmetry. The potassium ions are located on an 8*j* general position. The broadness of the diffraction peaks – indicating low crystallinity of the powder as well as the probable preferred orientation of the crystallites and the presence of some amorphous phases in **1** – did not allow the refinement of the atomic coordinates. The number of valence electrons (VEC) per $[Ta_6Br^i_{12}Br^a_6]^{2-}$ cluster unit is 16.
The Raman spectrum of the powder was recorded following the procedure given in supporting information (SI) and is given in Fig. 1. Numerous Raman-active vibrational modes are found below 300 cm^{-1}, with the most intense ones below 180 cm^{-1}.

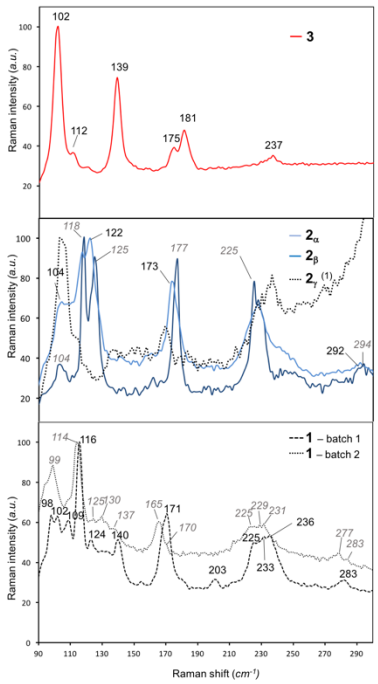

Fig. 1 Normalized Raman spectra of **1** (black, bottom panel) for two different batches with different ageing, of **3** (red, middle panel), and of $\mathbf{2}_\alpha$, $\mathbf{2}_\beta$, $\mathbf{2}_\gamma$ (blue, top panel). A different experimental setup was used for $\mathbf{2}_\gamma$ (SI); a baseline shift and rescaling of the intensity of the recorded spectrum was performed.

Compounds **2** are different hydrates obtained from dissolution of **1** according to different experimental protocols described in SI and summarized in Scheme 1. The X-ray powder diffraction investigations and TGA detailed in SI reveal that the compounds $\mathbf{2}_\alpha$, $\mathbf{2}_\beta$ and $\mathbf{2}_\gamma$ are structurally related with the structure of the $[\{Ta_6Cl^i_{12}\}Cl^a_2(H_2O)^a_4]\cdot 3H_2O$ analogous that was reported by Burbank *et al.*[33] As demonstrated below, $\mathbf{2}_\alpha$, $\mathbf{2}_\beta$ and $\mathbf{2}_\gamma$ are all based on a $[\{Ta_6Br^i_{12}\}Br^a_2(H_2O)^a_4]$ cluster units but they differ by their number of additional crystallization water molecules (respectively four and three for $\mathbf{2}_\beta$ and $\mathbf{2}_\gamma$ and more than four for $\mathbf{2}_\alpha$). As mentioned in Scheme 1, $\mathbf{2}_\delta$ is obtained by thermal treatment of $\mathbf{2}_\alpha$ and $\mathbf{2}_\beta$ and corresponds to a compound without crystallization water

molecules. The X-ray diffraction pattern recorded for $\mathbf{2}_\gamma$ is characterized by well-defined diffraction peaks which can be all indexed by considering the trigonal symmetry space group $P\overline{3}1m$ (No. 162) and the refined cell parameters a = 9.814(1) Å and c = 9.035(1) Å. High quality Rietveld refinement (Fig. S2) for $\mathbf{2}_\gamma$ can be reached by considering the structural model of the octahedral disordered cluster compound $[\{Ta_6Cl_{12}\}Cl_2(H_2O)_4]\cdot 3H_2O$ published by Burbank[33] for which chlorine atoms are replaced by bromine atoms.

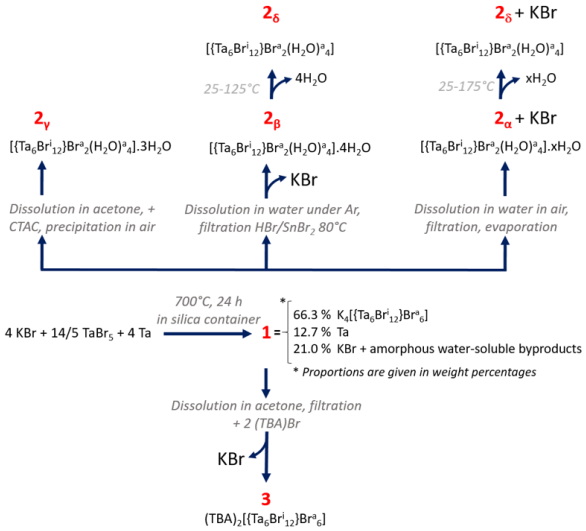

Scheme 1 Summary of the synthetic protocols

This suggests that $\mathbf{2}_\gamma$ is the bromide compound $[\{Ta_6Br_{12}\}Br_2(H_2O)_4]\cdot 3H_2O$ whose structure has never been reported before. The refined unit cell parameters are given in Table 1 and the refined atomic coordinates are gathered in the Table S1. The larger unit cell parameters refined for the bromide compound compared to those of the chloride compound (*i.e.* +4.8 % and +2.7 % for a and c parameters, respectively) are in fair agreement with the respective ionic radius of Br^- and Cl^-.[34] The cluster is centered on a $\overline{3}.m$ (D_{3h}) position. This symmetry is only apparent since it corresponds to the mean atomic positions of an orientation-disordered *trans*-$[\{Ta_6Br^i_{12}\}Br^a_2(H_2O)_4]^0$ cluster units which is in fact better described by a *pseudo*-D_{4h} symmetry. The number of valence electrons per $[\{Ta_6Br^i_{12}\}Br^a_2(H_2O)_4]^0$ cluster unit is 16, corresponding to the reduced form. The Ta_6 octahedron is flattened along the main axis ($\overline{3}$) and presents Br^- ligand in apical *trans* position (Table S1). These interatomic distances, gathered in the Table S2, allow to estimate that the average Ta-Br^a distance is roughly 2.8 Å which is particularly long. It has to be noted that the Br^a atoms are really close to the crystallization water molecules (shortest Br^a-$O(H_2)$ = 2.77 Å), suggesting that apical bromides are partially solvated by water, explaining the Ta-Br^a bonds weakening.

Table 1 Summary of refined crystallographic unit cell parameters reported in this work for $K_4Ta_6Br_{18}$, **2** $_\beta$ ($Ta_6Br_{12}Br_2(H_2O)_4.4\ H_2O$), **2** $_\gamma$ ($Ta_6Br_{12}Br_2(H_2O)_4.3\ H_2O$) and **3** ($(C_{16}H_{36}N)_2Ta_6Br_{18}$).

	$K_4Ta_6Br_{18}$	**2**$_\beta$	**2**$_\gamma$	**3**
Empirical formula	$K_4Ta_6Br_{18}$	$Ta_6Br_{12}Br_2(H_2O)_4.4\ H_2O$	$Ta_6Br_{12}Br_2(H_2O)_4.3\ H_2O$	$(C_{16}H_{36}N)_2Ta_6Br_{18}$
Crystal system	Monoclinic	Trigonal	Trigonal	Triclinic
Space group, Z	C2/m, 2	$P\bar{3}1m$, 1	$P\bar{3}1m$, 1	$P\bar{1}$, 1
a / Å	10.46(1)	9.765(1)	9.814(1)	9.2654(5)
b / Å	17.19(2)	9.765(1)	9.814(1)	13.2711(7)
c / Å	9.99(1)	9.090(2)	9.035(1)	13.5233(8)
α / °	90	90	90	66.127(2)
β / °	114.89(1)	90	90	81.129(2)
γ / °	90	90	90	89.119(2)
V / Å^3	1629.1(3)	750.7(2)	753.6(2)	1500.36(15)
Refinement method	XRPD, Le Bail refinement	XRPD, Le Bail refinement	XRPD, Rietveld refinement	Single-crystal X-ray
Reference	This work	This work	This work	Sokolov et al. [17]

The XRPD data recorded for **2**$_\beta$ on a large batch of powder evidence broad diffraction peaks at the same position (in 2θ) than those of **2**$_\gamma$, indicating the good purity of the sample (Fig. S2, Table 1). However, important discrepancies in term of peak intensities suggest a very high degree of disorder and microstructural defaults. The refined unit cell parameters are also slightly different and space group symmetry matching with XRPD data cannot be fully excluded. Considering the TGA experiments and chemical analysis of **2**$_\beta$ discussed in the SI, these variations are attributed to a difference in the number of crystallization water molecules (four and three for **2**$_\beta$ and **2**$_\gamma$ respectively). A comparison between XRPD of **2**$_\alpha$ and **2**$_\beta$ is given in Fig. S6. As summarized in Scheme 1, **2**$_\alpha$ is prepared by evaporation of a filtrated water solution of crude **1** which induces the unavoidable presence of KBr as impurity. Indeed, compared to the XRPD of **2**$_\beta$, the XRPD of **2**$_\alpha$ contains the supplementary peaks of the KBr salt. However, apart from these peaks, XRPD are highly similar. The main differences concern the relative intensities of the peaks and subtle displacements in 2θ. This can be reasonably interpreted by considering similar crystal structures based on the $[\{Ta_6Br^i_{12}\}Br^a_2(H_2O)^a_4]$ building block for both of **2**$_\alpha$ and **2**$_\beta$, but with slightly more water crystallization molecules per cluster unit. TGA experiments (Table S4) and chemical analysis enabled to formulate **2**$_\beta$ as $[\{Ta_6Br^i_{12}\}Br^a_2(H_2O)^a_4].4\ H_2O$ (%H exp: 0.71; %theo: 0.69). The temperature XRPD experiments (Fig. S6) indicate that **2**$_\alpha$ contain more crystallization water molecules than **2**$_\beta$ because of a higher temperature transition from **2**$_\alpha$ to **2**$_\delta$ than **2**$_\beta$ to **2**$_\delta$. TGA analysis of **2**$_\alpha$ indicates ten water crystallization molecules (SI) but it could not be confirmed by chemical analysis (%H exp: 0.58; %theo: 1.15 for 10 crystallization water molecules). Indeed, the presence of unavoidable KBr with **2**$_\alpha$ (Scheme 1) did not enable an accurate quantification of the number crystallization water molecules in **2**$_\alpha$. In summary, as soon as $K_4[\{Ta_6Br^i_{12}\}Br^a_6]$ is poured in water, the bromine apical ligands are exchanged by water molecules whatever the pH conditions (neutral or acidic). The structures of the resulting crystallized hydrates, *i.e.*, **2**$_\alpha$, **2**$_\beta$, and **2**$_\gamma$, are all based on $[\{Ta_6Br^i_{12}\}Br^a_2(H_2O)^a_4]$.

Raman spectra of **2**$_\alpha$, **2**$_\beta$ and **2**$_\gamma$ are given in Fig. 1. **2**$_\alpha$, **2**$_\beta$ present highly comparable Raman responses. The poor resolution of the spectrum of **2**$_\gamma$ prevents any quantitative analysis but allows to confirm the presence of preserved Ta_6 cluster units in the structure. The Raman spectrum of **2**$_\delta$ displays identical features as **2**$_\alpha$ and **2**$_\beta$ proving that the thermal treatment did not alter the $[\{Ta_6Br^i_{12}\}Br^a_2(H_2O)^a_4]$ cluster units (Fig. S8).

The compound **3**, $(TBA)_2[Ta_6Br^i_{12}Br^a_6]$ crystallizes in the $P\bar{1}$ space group (No. 2) with the refined unit cell parameters: a = 9.2654(5) Å, b = 13.2711(7) Å, c = 13.5233(8) Å, α = 66.127(2)°, β = 81.129(2)°, γ = 89.119(2)°. This X-ray diffraction analysis performed on single crystal confirms that **3** corresponds to the structure 5c reported by Sokolov *et al.* in ref 17 (Table 1). The structure of **3** is based on a distorted body-centered stacking of $[\{Ta_6Br^i_{12}\}Br^a_6]^{2-}$ cluster units. The TBA^+ cations are located in the voids formed by the cluster framework. The cluster units are centered on the 1*a* Wyckoff position and exhibit the C_i symmetry. The number of valence electrons per $[Ta_6Br^i_{12}Br^a_6]^{2-}$ cluster unit (VEC) is 14.

The Raman spectrum of the powder of **3** is given in Fig. 1. It is noticeably different (number energies and intensities of the peaks) from the spectra of **2**$_\alpha$, **2**$_\beta$ which are highly comparable (Fig. 1). The two main distinctions between them are the absence of peaks above 240 cm^{-1} in the Raman spectrum of **3** and the presence of an intense peak at 140 cm^{-1} that is not present in **2**$_\alpha$, **2**$_\beta$ spectra. The Raman spectra of **1** shows numerous sharp peaks some at the same energies than in **3** and **2**$_\alpha$, **2**$_\beta$ spectra but of different intensities and some additional ones. Interestingly, Raman spectra of **1** prepared using the same experimental protocol in slightly different atmospheric and ageing conditions show differences in the relative intensities of the peaks (Fig. 1, batch 1 and 2). The description and indexation of these experimental Raman spectra is provided together with the computational simulation results in the computational section to avoid repetition.

Mass spectrometry analyses, electrochemical properties and UV-visible absorption spectra of the solutions of 1, 2 and 3 in water, acetone and dichloromethane.

Solubilization in water, acetone and dichloromethane. The methodology is detailed in SI. It has to be pointed out that **1** is insoluble in dichloromethane (DCM) while $\mathbf{2}_{\beta}$ is insoluble both in acetone and DCM, respectively. As detailed previously, acetone solutions of **1** in the absence of O_2 are green but turn instantly to brown when handled in air (solution labelled $\mathbf{1}_{acetone}$). **3** behaves differently since it readily dissolves both in acetone and DCM. These solutions will be referred as $\mathbf{3}_{acetone}$ and $\mathbf{3}_{DCM}$. The increased solubility of **3** in organic solvent compared to **1** is explained by the presence of TBA^+ counter cations which are known to increase solubility in non-aqueous solvents. We have indeed observed that addition of a few drops of water in freshly prepared acetone solutions leads to gradual bleaching of the colored initial solutions and appearance of a white precipitate. Since water and DCM are not miscible, no such effect is observed when adding traces of water to $\mathbf{3}_{DCM}$.

Mass spectrometry analyses. The mass spectra obtained for solutions of **1** in water and acetone, $\mathbf{2}_{\beta}$ in water, and **3** in DCM and acetone, are represented in Fig. 2. The list of detected ions is summarized in Table 2. The most abundant negative ions that are detected by mass spectrometry analyses of the freshly prepared $\mathbf{1}_{acetone}$, $\mathbf{3}_{acetone}$ and $\mathbf{3}_{DCM}$ solutions (Fig. 2, Table 2) are $[\{Ta_6Br_{12}\}Br_6]^{2-}$ and $[\{Ta_6Br_{12}\}Br_5]^{2-}$. This allows to conclude that i) the change of colour of $\mathbf{1}_{acetone}$ from green to brown is due to oxidation and that ii) the bromine apical ligands are preserved in aprotic solvents even though traces of hydrolysed clusters of $[\{Ta_6Br_{12}\}Br_5(H_2O)(OH)]^{2-}$ are detected. The negatively-charged $[\{Ta_6Br_{12}\}Br_4]^{2-}$ and $[\{Ta_6Br_{12}\}Br_3]^{-}$ are also detected $\mathbf{3}_{acetone}$. The TBA-adduct $[(TBA)\{Ta_6Br_{12}\}Br_5]^{-}$ is also found in both solutions of **3**. The detection of $[\{Ta_6Br_{12}\}Br_5(H_2O)(OH)]^{2-}$, $[\{Ta_6Br_{12}\}Br_5(OH)_2]^{2-}$, $[\{Ta_6Br_{12}\}Br_5(OH)_2O]^{2-}$, $[\{Ta_6Br_{12}\}Br_6H]^{2-}$, $[\{Ta_6Br_{12}\}Br_6O]^{2-}$ and positively charged mononuclear tantalum ions in $\mathbf{3}_{acetone}$ and $\mathbf{3}_{DCM}$, and their increase over time, clearly indicates the sensitivity of $[\{Ta_6Br_{12}\}Br_6]^{2-}$ to H_2O (even traces) in these organic solvent reflected by the gradual bleaching and appearance of a white aqua-hydroxo Ta^V-based precipitate.

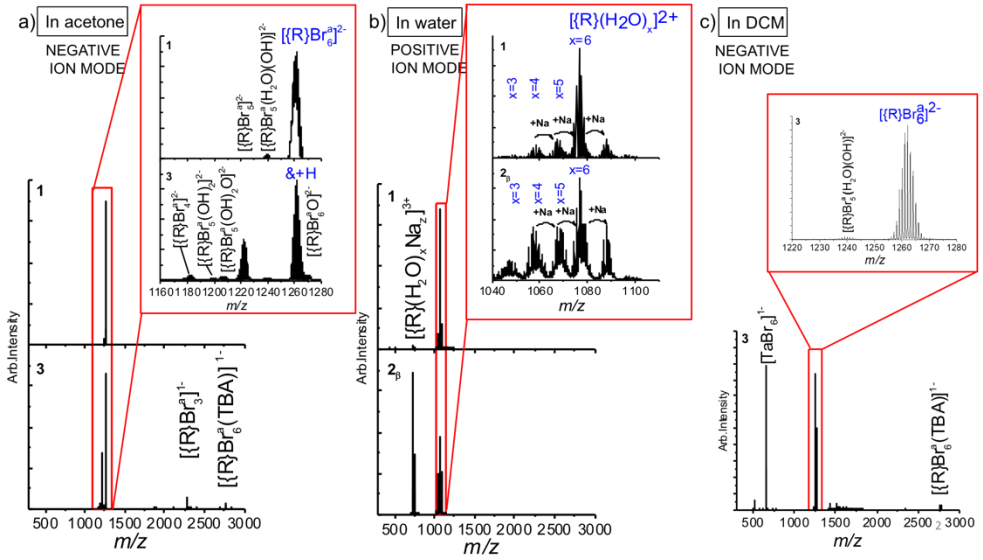

Fig. 2 a) Comparison of the mass spectra of solutions of **1** and **3** in acetone in negative mode. c) Comparison of the spectra of **1** and $\mathbf{2}_{\beta}$ in water in positive mode. c) Mass spectrum of solution of **3** in dichloromethane (DCM) in negative mode. {R} corresponds to the core $\{Ta_6Br^i_{12}\}$.

Water solutions of **1** and $\mathbf{2}_{\beta}$ were also investigated by mass spectrometry ($\mathbf{1}_{water}$ and $\mathbf{2}_{\beta\text{-water}}$). Interestingly, only positive ions are detected (Table 2, Fig. 2). The most abundant species on the mass spectra are, in both cases, species in which six bromide are exchanged with water. It likely corresponds to species where the $\{Ta_6Br^i_{12}\}$ core is preserved and all apical bromides are replaced with H_2O (*i.e.* $[\{Ta_6Br_{12}\}(H_2O)_6]^{2+}$). Less abundant ions are detected with an equal number of bromides but only three, four or five water molecules: they are likely to be resulting from one to three water molecules loss from the most intense fully hydrated species. Only ionic fragments can be detected by mass spectrometry techniques thus the existence of neutral fragments like $[\{Ta_6Br_{12}\}(H_2O)_4(OH)_2]$ in solution cannot be excluded. Subsequent recordings have shown that ions distribution measured from these water solutions are stable over time. Sodium adducts of formula $[\{Ta_6Br_{12}\}(H_2O)_xNa]^{2+}$ and $[\{Ta_6Br_{12}\}(H_2O)_yNa_z]^{2+}$, $4 < y < 6$; $z = 3, 4$ are also detected. The detection of $[(Ta_6Br_{12})(H_2O)_n]^{2+}$ fragments in $\mathbf{1}_{water}$ and $\mathbf{2}_{\beta\text{-water}}$ implies that all apical bromines of the initial $[\{Ta_6Br_{12}\}Br_6]^{4-}$ (**1**) and $[\{Ta_6Br_{12}\}Br_2(H_2O)^a_4]$ (**2**) cluster units present in the crystal structure have been replaced by water molecules. This is supported by the absence of $[\{Ta_6Br_{12}\}Br_6]^{n-}$ ions and subsequent fragments in negative mode.

Electrochemical properties. The electrochemical measurements of $\{Ta_6Br_{12}\}^{2+}$-containing cluster solution that are available to date were performed in perchloric acid aqueous media.[35] Addition of acid is mandatory to measure the redox properties of $[\{Ta_6Br_{12}\}(H_2O)_6]^{2+}$ alone by preventing the formation of aqua hydroxo species $[\{Ta_6Br_{12}\}(H_2O)_x(OH)_{6-x}]^{n-/m+}$. Indeed, the $[\{Ta_6Br_{12}\}(H_2O)_6]^{2+}$ cluster units are in equilibrium with $[\{Ta_6Br_{12}\}(H_2O)_x(OH)_{6-x}]^{n-/m+}$ and H_3O^+ species. As already discussed by Hughbanks *et. al.* for parent centered zirconium clusters,[36] hydrated tantalum cluster species act as weak acid *via* deprotonation of water ligands. In order to evaluate the possible Brønsted acidic property of $[\{Ta_6Br_{12}\}(H_2O)_6]^{2+}$, we have performed a titration

of a 1.2 10^{-3} mol.L^{-1} fresh aqueous solution of $\mathbf{2}_{\beta}$ (pH before titration after dissolution ≈ 3.5). The first pKa was estimated at 3.9. The determination of the pKa values for the second and the upper acidities were not possible because of the partial to full precipitation of $[\{Ta_6Br_{12}\}(H_2O)_x(OH)_{6-x}]^{n-/m+}$ species with pH increase.

Table 2 List of ions detected by mass spectrometry analysis of solutions of **1** and $\mathbf{2}_{\beta}$ and **3** in different solvents

Compounds 1 and 3 *in acetone*	
Positive ion mode	<u>specific for 3:</u> $[(TBA)_2TaBr_2O]^+$ $[(TBA)_2TaBr_4O]^+$ (TBA)TaBr aggregates
Negative ion mode	$[\{Ta_6Br_{12}\}Br_6]^{2-}$ $[\{Ta_6Br_{12}\}Br_5]^{2-}$ $[\{Ta_6Br_{12}\}Br_5(H_2O)(OH)]^{2-}$ <u>specific for 3:</u> $[\{Ta_6Br_{12}\}Br_6O]^{2-}$ $[\{Ta_6Br_{12}\}Br_6H]^{2-}$ $[\{Ta_6Br_{12}\}Br_4]^{2-}$ $[\{Ta_6Br_{12}\}Br_4(OH)_2]^{2-}$ $[\{Ta_6Br_{12}\}Br_4(OH)_2O]^{2-}$ $[\{Ta_6Br_{12}\}Br_3]^{-}$ $[(TBA)\{Ta_6Br_{12}\}Br_5]^{-}$
Compounds 1 and $\mathbf{2}_{\beta}$ *in water*	
Positive ion mode	$[\{Ta_6Br_{12}\}(H_2O)_x]^{2+}$; 3 < x < 6 $[\{Ta_6Br_{12}\}(H_2O)_xNa]^{2+}$; 4 < x < 6 $[\{Ta_6Br_{12}\}(H_2O)_xNa_z]^{3+}$; 4 < x < 6; z = 3, 4; Na-containing oligomers
Negative ion mode	No signal
Compound 3 *in DCM*	
Positive ion mode	$[(TBA)_2TaBr_2O]^+$ $[(TBA)_2TaBr_4O]^+$ (TBA)TaBr aggregates
Negative ion mode	$[\{Ta_6Br_{12}\}Br_6]^{2-}$ $[(TBA)\{Ta_6Br_{12}\}Br_5]^{1-}$ $[\{Ta_6Br_{12}\}Br_5(H_2O)(OH)]^{2-}$

The cyclic voltammetry curves of aqueous solutions of $[\{Ta_6Br_{12}\}(H_2O)_6]^{2+}$ at pH = 1 show two consecutive and reversible one-electron transfer processes at 0.35 V and 0.65 V vs SCE (0.598 V and 0.898 V vs SHE) that were attributed to the oxidation of the $\{Ta_6Br_{12}\}^{2+}$ cluster core firstly into $\{Ta_6Br_{12}\}^{3+}$ and then into $\{Ta_6Br_{12}\}^{4+}$-containing species, respectively.[35] Considering the mass spectrometry study detailed herein for $\mathbf{2}_{\beta}$ in water, the measured redox potentials and the electrochemical behavior correspond to those of $[Ta_6Br^{i}_{12}(H_2O)^{a}_6]^{n+}$ cluster unit, *i.e.* $\{Ta_6Br_{12}\}^{2+}$ clusters complexed with apical H_2O ligands.

In order to acquire new knowledge about the electrochemistry of cluster-based tantalum bromides, we carried out electrochemical characterizations of solutions of $(TBA)_2[\{Ta_6Br_{12}\}Br_6]$ (**3**) in a non-aqueous solvent, i.e. DCM (Fig. 3). The choice of the solvent is of prime importance to avoid artefacts: i) it must be a non-coordinating solvent, 2) it must prevent exchanges of apical bromine by water molecules or hydroxo groups (H_2O coming for **1** or present as traces in the solvent). Consequently, the compatible solvents are limited since usual solvent like acetonitrile, alcohols, DMF, acetone are outlawed. The cyclic voltammogram was recorded by applying an anodic sweep (from positive to negative potentials). In $\mathbf{3}_{DCM}$, the $\{Ta_6Br_{12}\}^{n+}$ cluster-cores are bonded to apical bromide ligands. Consequently, $[\{Ta_6Br_{12}\}Br^{a}_6]^{4-}$, $[\{Ta_6Br_{12}\}Br^{a}_6]^{3-}$ and $[\{Ta_6Br_{12}\}Br^{a}_6]^{2-}$ cluster are associated to $\{Ta_6Br_{12}\}^{2+}$, $\{Ta_6Br_{12}\}^{3+}$ and $\{Ta_6Br_{12}\}^{4+}$ cluster-cores respectively. For sake of comparison between the present electrochemistry study performed in organic media with the previously published studies performed in aqueous media, the following description will focus on the evolution of the charge of the $\{Ta_6Br_{12}\}^{n+}$ cluster-cores upon variation of the applied electric potential. The previous electrochemical studies on $\{Ta_6Br^{i}_{12}\}$-containing systems[7, 14, 15, 37] in water at low pH value established that the initial redox state of the $\{Ta_6Br_{12}\}^{n+}$ species at equilibrium potential was 3+ corresponding to a VEC of 15. In this study, starting from $[\{Ta_6Br_{12}\}Br_6]^{2-}$ in DCM, the initial redox state of the $\{Ta_6Br^{i}_{12}\}^{n+}$ species at equilibrium potential is 4+ (*i.e.* VEC = 14; $\{Ta_6Br_{12}\}^{4+}$ cluster core).

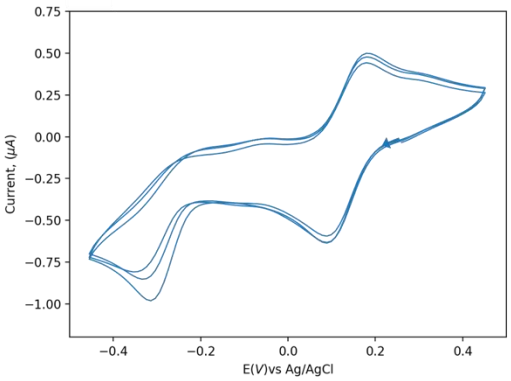

Fig. 3 The cyclic voltammogram of 1.10^{-3} M of **3** in DCM (1.10^{-1} M of (TBA)[PF_6]) recorded starting by applying an anodic sweep.

$$\{Ta_6Br_{12}\}^{4+} + e^- \rightarrow \{Ta_6Br_{12}\}^{3+} \qquad \text{Eq. 1}$$

$$\{Ta_6Br_{12}\}^{3+} + e^- \rightarrow \{Ta_6Br_{12}\}^{2+} \qquad \text{Eq. 2}$$

One reversible one-electron transfer process is clearly observed around 0.13 V vs Ag/AgCl ($E_{1,ox}$ = 0.18 V vs Ag/AgCl, $E_{1,red}$ = 0.09 V vs Ag/AgCl). This redox process is attributed to the reversible reduction of a $\{Ta_6Br_{12}\}^{4+}$-core species to a $\{Ta_6Br_{12}\}^{3+}$-core species following the reaction Eq. 1. A quasi non-reversible one electron transfer is observed around -0.18 V (-0.017 V vs ESH). It corresponds to a well-defined cathodic peak located at $E_{2,red}$ = -0.32 V vs Ag/AgCl (-0.123 V vs ESH) which is attributed to the reduction of $\{Ta_6Br_{12}\}^{3+}$ core into $\{Ta_6Br_{12}\}^{2+}$ (Eq. 2). However, the anodic peak corresponding to the reverse oxidation reaction around $E_{2,ox}$ = -0.05 V vs Ag/AgCl (0.147 V vs ESH) is very weak. This cathodic peak decreases over cycles whereas the current of the reversible redox process around 0.13 V vs Ag/AgCl remains stable (0.327 V vs ESH). This is concomitant with the formation of a green precipitate, which green emerald color is characteristic of $\{Ta_6Br_{12}\}^{2+}$-based compounds, on the reference electrode and in the solution. Thus, we can explain this electrochemical behavior by the non-solubility of the $\{Ta_6Br_{12}\}^{2+}$-species in DCM. The precipitation of the green $\{Ta_6Br_{12}\}^{2+}$-based compound leads to the modification of the surface of the working electrode. This precipitation must correspond to the formation of $(TBA)_4[\{Ta_6Br_{12}\}Br_6]$ since on one hand, in organic solution apical ligands are not exchanged and since, on the other hand, the single species of cations is $(TBA)^+$. The co-precipitation of aqua or hydroxo cluster (VEC = 16) based species cannot be excluded on the basis of species detected by mass spectrometry of $\mathbf{3}_{DCM}$. This alteration of the working electrode limits the charge transfer of the reduction of $\{Ta_6Br_{12}\}^{3+}$ cluster-cores causing the decrease of the cathodic current at -0.05 V vs Ag/AgCl. However, it does not drastically affect the reversible redox reaction between the $\{Ta_6Br_{12}\}^{3+}$ and $\{Ta_6Br_{12}\}^{4+}$-based species at 0.13 V vs Ag/AgCl (0.327 V vs ESH).

Additionally, it is important to note that the potential values involved in redox reactions (Eq. 1 and Eq. 2) in DCM are very different from those reported for the same reactions of the $\{Ta_6Br_{12}\}^{2+}$ cluster core carried out in acidified aqueous media. In order to compare all the data, it must be taken into account that the reference electrodes are ECS in the previous works (0.197 V vs ESH) in acidic solutions[35] while Ag/AgCl electrode (0.248 V vs ESH) was used in the present work. Consequently, the normalized potential considering SHE as reference are 0.598 V and 0.898 V in water[35] and -0.018 V and 0.327 V in DCM (this work). The negative shift of the oxidation potential of about 0.6 V from water to DCM has at least two origins: the nature of the electrolyte and the difference in the nature of apical ligands. If a negative shift in organic media compared with that observed in the aqueous medium is usual, a strong shift of 0.6 V cannot be the single reason. Indeed, in organic solvent, $\{Ta_6Br_{12}\}^{2+}$ is bonded to bromine ligands ($[\{Ta_6Br_{12}\}Br_6]^{n-}$) while the cluster units are $[\{Ta_6Br_{12}\}(H_2O)_6]^{n+}$ in acidified aqueous media.

UV-visible absorption properties. The normalized UV-visible absorption spectra of solutions of **1** and $\mathbf{2}_\beta$ in water and a solution of **1** in acetone ($\mathbf{1}_{acetone}$) are shown in Fig. 4. As stressed above, the freshly prepared $\mathbf{1}_{acetone}$ is green but turns to brown when exposed to air. $\mathbf{1}_{water}$ solution is green and does not evolve with time. It is worth pointing out that the spectra of $\mathbf{1}_{water}$ and $\mathbf{2}_{\beta\text{-water}}$ are superimposable. This observation fully corroborates the mass spectrometry results. They show two quite intense and quite asymmetrically-shaped bands in the visible (vis) region. Their maxima are centered at 640 and 746 nm. Even though not very intense, continuous absorption is measured over the complete range of excitation wavelengths. The main absorption peaks in the UV region are found at 388 nm for $\mathbf{1}_{acetone}$ and 352 nm for $\mathbf{1}_{water}$ and $\mathbf{2}_{\beta\text{-water}}$. A large low-energy band spreading between around 900-1000 nm is observed in $\mathbf{1}_{acetone}$ spectrum but it does not exist in $\mathbf{1}_{water}$ centered at 932 nm. For comparison, absorption spectra of solutions of **1** dissolved in methanol and in ethanol were also recorded (Fig. S9). Interestingly, they highly resemble to the spectrum of $\mathbf{1}_{water}$.

Additional experiments were performed by adding $Fe(NO_3)_3$ and $SnBr_2$ salts to the $\mathbf{1}_{water}$ solution as oxidizing and reducing agents respectively (Fig. S10). In the first case, the bands centered at 640 and 746 nm are diminishing together with the increase of the $Fe(NO_3)_3$ concentration. This is concomitant with the appearance of two new peaks at roughly 717 nm and 878 nm which are attributed to the appearance of $[\{Ta_6Br^i_{12}\}(H_2O)_6]^{3+}$ cluster units in solution (VEC = 15) and the disappearance of

$[\{Ta_6Br^i_{12}\}(H_2O)_6]^{2+}$. The addition of $SnBr_2$ to $\mathbf{1}_{water}$ hardly modifies the absorption spectra confirming the $\{Ta_6Br^i_{12}\}^{2+}$ cluster core of VEC = 16 in the starting solution $\mathbf{1}_{water}$ as also revealed by mass spectrometry ($[\{Ta_6Br^i_{12}\}(H_2O)_6]^{2+}$ ion detection). The obtained spectra for $[\{Ta_6Br^i_{12}\}(H_2O)_6]^{2+}$ and $[\{Ta_6Br^i_{12}\}(H_2O)_6]^{3+}$ look like those already reported by B. Spreckelmeyer *et al*.[38] In this work, an HBr acidified aqueous solution of $[\{Ta_6Br^i_{12}\}(H_2O)^a_6]^{2+}$ ions was oxidized by $KBrO_3$.

The normalized UV-visible absorption spectra of solutions of **3** in acetone and DCM are represented in Fig. 4. They are highly similar showing a continuous absorption from UV to visible and from 820 to 1200 nm. The band maxima are located at 391/393, 462/468, 540/548, 922/947 and 1104/1121 nm ($\mathbf{3}_{DCM}$/$\mathbf{3}_{acetone}$). The band maximum shifts from $\mathbf{3}_{acetone}$ to $\mathbf{3}_{DCM}$ are attributed to slight differences in solvation effects between acetone and DCM. Interestingly, these spectra are similar to that of $\mathbf{1}_{acetone}$ (Fig. 4, left) which is only differentiated by the presence of a supplementary low-intensity peak at 752 nm. From these analyses, it is reasonable to attribute the absorption properties of $\mathbf{3}_{acetone}$ to $\mathbf{3}_{DCM}$ to $[\{Ta_6Br^i_{12}\}Br^a_6]^{2-}$ cluster units with a VEC = 14 (slight variation depending on the organic solvent used). The supplementary band at 752 nm found for $\mathbf{1}_{acetone}$ could be attributed to the presence of traces of $[\{Ta_6Br^i_{12}\}Br^a_6]^{3-}$ (VEC = 15).

The absorption properties in the 600 nm – 1200 nm region of the solutions of $\{Ta_6Br^i_{12}\}$-based units reveal to be mostly influenced by the oxidation state of the $\{Ta_6Br^i_{12}\}^{m+}$ cluster core rather than by the nature of apical ligands. The intense absorption bands with maxima located around 640 and 750 nm are characteristic of $\{Ta_6Br^i_{12}\}^{2+}$ cluster core (VEC = 16). After oxidization of $\{Ta_6Br^i_{12}\}^{2+}$ by addition of $Fe(NO_3)_3$ in $\mathbf{1}_{water}$, the new absorption bands at roughly 717 nm and 878 nm can be attributed to the presence of the $\{Ta_6Br^i_{12}\}^{3+}$ cluster core (VEC = 15). For the $\{Ta_6Br^i_{12}\}^{4+}$ cluster core (VEC = 14), a continuous absorption is observed on the spectra of $\mathbf{3}_{DCM}$ and $\mathbf{3}_{acetone}$ from 800 nm to 1200 nm with respectively two band maxima located at 930 and 1150 nm. The region ranging from UV to 600 nm, the differences in the spectra are less obvious to exploit them on the bases of obvious differentiations (Fig. S10).

Computational results – electronic structures, calculated Raman optical activities, UV-visible absorption properties of selected cluster units.

The $[\{M_6L^i_{12}\}L^a_6]$ cluster units (M = Nb and Ta) have been intensively studied on a computational point of view.[39-41] The MO energy diagram of $[\{M_6L^i_{12}\}L^a_6]$ cluster unit levels in the Fermi region is generally described as a set of eight highest occupied molecular orbitals (HOMOs) presenting metal–metal bonding character and metal–ligand antibonding character to a lesser extent which is separated by a significant energy gap from a set of 16 unoccupied MOs (LUMOs). These LUMOs show mainly a metal–metal anti-bonding character.

The geometrical arrangement of $[\{Ta_6Br^i_{12}\}Br^a_6]^{n-}$ units (n = 2, 3, 4) were optimized at the level of theory described in the computational details in the SI. At this level of theory, the three systems are presenting an O_h symmetry (calculations in vacuum, at 0 K). The main calculated distances are given in Table 3 together with selected experimental solid-state data issued from X-ray diffraction studies. The calculated Ta-Ta and Ta-Br bond lengths agree reasonably well with the experimental data with a maximum of deviation of 3 %. This level of accuracy is comparable to the most recent studies performed in the parent Nb series.[41] In the $[\{Ta_6Br^i_{12}\}Br^a_6]^{n-}$ series, the calculated Ta-Ta distances increase by 0.054 Å upon one-electron oxidation from VEC = 16 (n = 4) to VEC =15 (n = 3) and increase by 0.045 Å from VEC = 15 to VEC =14 (n = 2). Concomitantly, the Ta-Br^i decreases by 0.018 Å at each oxidation step. The Ta-Br^a distances decrease more importantly (-0.132 Å and -0.094 Å going from n = 4 to 3 and to 2). Oxidation corresponds to the formal depopulation of the HOMOs of the molecular system followed by an electronic and atomic relaxation. The loss of the Ta-Ta bonding and Ta-Br^i antibonding characters upon depopulation leads to the lengthening and the shortening of the associated bond lengths respectively, in agreement with experimental data (Table 3).[42]

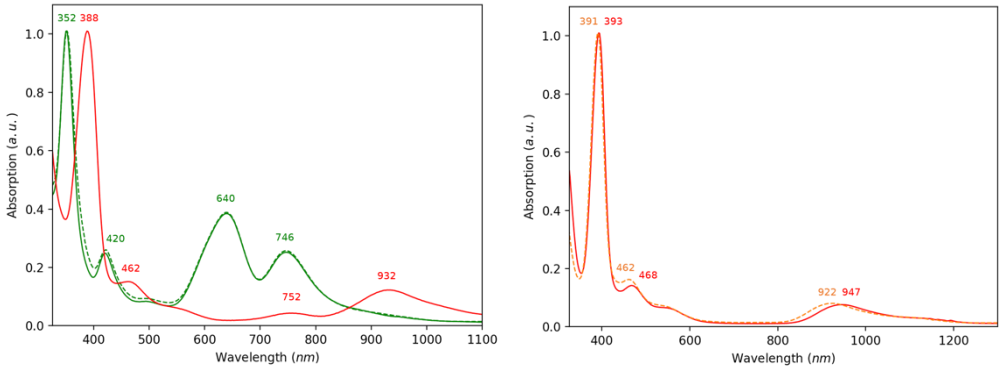

Fig. 4 Normalized UV-visible absorption spectra of: left) $\mathbf{1}_{acetone}$ (red), $\mathbf{1}_{water}$ (green) and $\mathbf{2}_{\beta\text{-}water}$ (dotted green) at RT; right) **3** in acetone (red) and **3** in DCM (dotted orange).

For the aqua-clusters, the geometrical arrangements of the aqua-$[\{Ta_6Br^i_{12}\}(H_2O)^a_6]^{n+}$ (n = 4, 2) and hydroxo-$[\{Ta_6Br^i_{12}\}(OH)^a_6]^{4-}$ units as well as those of $[\{Ta_6Br^i_{12}\}(H_2O)^a_{6-x}(OH)_x]^{m+}$ (x = 1, 2; m = 1, 0) aqua-hydroxo-intermediates were optimized using the same approach as that used for $[\{Ta_6Br^i_{12}\}Br^a_6]^{n-}$ units (n = 2, 3, 4). It turns out that the direct comparison between experimental

solid-state geometries and calculated metrics of these cluster units reported in the literature is problematic. Indeed, numerous hydrogen bond-type interactions are found in the reported solid-state structures between water solvent molecules, counterions, and ligands of the cluster.[43] The O-H bond distances of the H_2O apical ligands can thus be intermediate between the two extrema, aquo and hydroxo ligands. Ta-O(H_x) bonds are consequently importantly affected.
This can be seen by comparing the experimental structures of $Cs[\{Ta_6Br^i_{12}\}(H_2O)^a_6]Br_3{\cdot}6H_2O$ and $[\{Ta_6Br^i_{12}\}(H_2O)^a_6]Cl_2{\cdot}8H_2O$ which main characteristics are reported in Table 2.[17] Even, if they present the same cluster unit chemical formula $[\{Ta_6Br^i_{12}\}(H_2O)^a_6]^{2+}$, the Ta-O($H_x$) mean value is 2.251(5) Å for the former (at 296 K) and 2.377(2) for the latter (at 91 K).

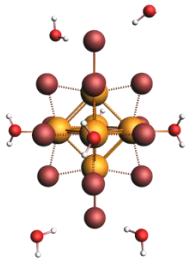

Fig. 5 Optimized geometry of the model [*trans*-$\{Ta_6Br^i_{12}\}Br^a_2(H_2O)^a_4$] + 4 H_2O.

Such a variation cannot be explained by a factor of temperature only and is undoubtedly due to disparities in the solid-state environments of the cluster units. On the basis of our computational results in which the Ta-O(H_x) bond lengths are 2.402 Å in $[\{Ta_6Br^i_{12}\}(H_2O)^a_6]^{2+}$ units and 2.120 Å in hydroxo series $[\{Ta_6Br^i_{12}\}(OH)^a_6]^{4-}$ (same VEC = 16), we can conclude from the analysis of the experimental metrics that hydrogen atoms of the H_2O apical ligands in $Cs[\{Ta_6Br^i_{12}\}(H_2O)^a_6]Br_3{\cdot}6H_2O$ should be more involved in hydrogen bonding interactions than in $[\{Ta_6Br^i_{12}\}(H_2O)^a_6]Cl_2{\cdot}8H_2O$.[17] A wide range of intermediate distances are thus possible in the different crystal structures as revealed by the computational study performed on $[\{Ta_6Br^i_{12}\}(H_2O)^a_{6-x}(OH)_x]^{m+/n-}$ series.[44]
Among $\mathbf{2}_{\alpha,\beta,\gamma}$ series, only the $\mathbf{2}_\gamma$ solid-state structure could be determined experimentally but the geometry of the cluster units could not be accurately refined because of their orientation disorder. To complete experimental investigations, we have calculated in the optimized geometry the [*trans*-$\{Ta_6Br^i_{12}\}Br^a_2(H_2O)^a_4$] which main geometrical data are given in Table 3. The Ta-Br^i distances are particularly short compared to the calculated value for a fully brominated system (2.689 Å) and to the experimental estimation of 2.80 Å. This discrepancy reveals that intramolecular interactions play an important role at the solid-state and that they should be simulated to allow comparison between solid-state experimental measurements and the calculated ones. We thus explicitly included the four crystallization H_2O molecules that surround the bromine apical ligands in the crystal structure of $\mathbf{2}_\gamma$ (Fig. 5). This initial guess geometry [*trans*-$\{Ta_6Br^i_{12}\}Br^a_2(H_2O)^a_4$] + 4 H_2O was optimized using Grimme dispersion corrections to take into account long-range interactions, *i.e.* hydrogen bonding. The main computed distances are given in Table 3. Interestingly, the $\{Ta_6Br^i_{12}\}^{2+}$ core was kept unchanged upon this modification while the Ta-Br^a bond lengths were elongated to reach 2.814 Å and the Ta-O(H_2) are shortened by 0.087 Å. The hydrogen bonds between the H_2O molecules and the [*trans*-$\{Ta_6Br^i_{12}\}Br^a_2(H_2O)^a_4$] cluster weaken importantly the Ta-Br^a bonds as observed experimentally.

Table 3. Main bond lengths (Å) of the optimized geometries $[\{Ta_6Br^i_{12}\}Br^a_6]^{4-}$ (n = 2-4) (O_h symmetry), $[\{Ta_6Br^i_{12}\}(H_2O)^a_4]^{2+/4+}$, $\{Ta_6Br^i_{12}\}(Br)^a_2(H_2O)^a_4$, $[\{Ta_6Br^i_{12}\}(Br)^a_2(H_2O)^a_4]+4H_2O$, $[\{Ta_6Br^i_{12}\}(OH)^a_6]^{4-/2-}$, $[\{Ta_6Br^i_{12}\}(OH_2)^a_6]^{2+}$. Average distances are given if the differences are of less than 1%, range of distances are given otherwise. Available experimental X-ray structures are given for sake of comparison.

DFT optimized clusters	VEC	Ta-Ta	Ta-Br^i	Ta-Br^a	Ta-$O^a(H_2)$	Ta-$O^a(H)$
$[\{Ta_6Br^i_{12}\}Br^a_6]^{4-}$	16	2.963	2.646	2.985		
$[\{Ta_6Br^i_{12}\}Br^a_6]^{3-}$	15	3.017	2.628	2.853		
$[\{Ta_6Br^i_{12}\}Br^a_6]^{2-}$	14	3.062	2.618	2.759		
$[\{Ta_6Br^i_{12}\}(H_2O)^a_4]^{2+}$	16	2.857 (×8) - 2.941 (×4 basal)	2.632 - 2.668		2.380	
$[\{Ta_6Br^i_{12}\}$*trans*-$Br^a_2(H_2O)^a_4]$	16	2.950 (×8) - 2.873 (×4 basal)		2.689	2.455	
$[\{Ta_6Br^i_{12}\}$*trans*-$Br^a_2(H_2O)^a_4]+4H_2O$ grimme	16	2.905 - 2.917 (×8) - 2.873 (×4 basal)	2.617 - 2.647	2.814	2.368	
$[\{Ta_6Br^i_{12}\}(H_2O)^a_6]^{2+}$	16	2.906	2.637 - 2.662		2.402	
$[\{Ta_6Br^i_{12}\}(OH)^a_6]^{4-}$	16	3.007	2.678 - 2.777			2.120
$[\{Ta_6Br^i_{12}\}(OH)^a_6]^{2-}$	14	3.060 (×6) 3.108 (×6)	2.652 - 2.675			2.074
Selected experimental structures	VEC	Ta-Ta	Ta-Br^i	Ta-Br^a	Ta-$O^a(H_2)$	Ta-$O^a(H)$
$CsEr[\{Ta_6Br^i_{12}\}Br^a_6]$ ref 43 (295 K)	16	2.898(6)	2.587(7)	2.89(1)		
$(TBA)_2[\{Ta_6Br^i_{12}\}Br^a_6]$ ref 17 (150 K)	14	3.027(7)	2.565(9)	2.70(1)		
$CsBr\cdot[\{Ta_6Br^i_{12}\}(H_2O)^a_6]Br_2\cdot 6H_2O$; ref 17 (296 K)	16	2.899(5)	2.605(6)		2.251(5)	
$[\{Ta_6Br^i_{12}\}(H_2O)^a_6]Cl_2.8H_2O$; ref 17 (91 K)	16	2.940(1)	2.588(1)		2.377(2)	

Raman active vibrational frequencies were calculated using the experimental $[\{Ta_6Br^i_{12}\}Br^a_6]^{2-/4-}$ for $K_4[\{Ta_6Br^i_{12}\}Br^a_6]$ and **3** and their optimized geometries. Their differences in bond lengths and deviations from O_h symmetry modify noticeably the simulated Raman results. For $[\{Ta_6Br^i_{12}\}Br^a_6]^{4-}$, the simulated Raman spectra are given in Fig. S11 for both, the geometry issued from the X-ray solid-state structure, and the optimized one (see Table 3). The distances being overall longer in the optimized O_h structure and the symmetry lowered to D_{3h}, a global shift to lower vibrational frequencies is calculated (overall roughly -20 cm^{-1}) but the vibrational motions are maintained. The relative intensities are also slightly modified but the results are qualitatively similar. The same trend was found for $[\{Ta_6Br^i_{12}\}Br^a_6]^{2-}$ (experimental symmetry C_i). For sake of comparison, the experimental Raman spectra of **1** and **3** are compared to the simulation performed using the geometries of structures based on $[\{Ta_6Br^i_{12}\}Br^a_6]^{2-/4-}$ cluster units that were determined by single crystal X-ray diffraction techniques (Fig. 6).

At first sight, the agreement between the simulated Raman spectra of $[\{Ta_6Br^i_{12}\}Br^a_6]^{4-}$ and the experimental spectra of **1** is poor. As detailed below, the surface of the powder of **1** is particularly sensitive to oxidation and hydrolysis. Moreover, the sensitivity of Raman spectroscopy is very high since it probes the surface of the sample which does not reflect the macroscopic composition of the sample as does for instance X-ray powder diffraction detailed above. Consequently, the experimental spectra is most probably a combination of several Raman signatures among which $[\{Ta_6Br^i_{12}\}Br^a_6]^{2-/4-}$ and $[$*trans*-$\{Ta_6Br^i_{12}\}$ $Br^a_2(H_2O)^a_4]$ which are probably the most abundant at the surface of the sample. For $[\{Ta_6Br^i_{12}\}Br^a_6]^{4-}$, the calculation allows to identify the vibrational modes which are forming the band between 115 cm^{-1} and 120 cm^{-1} (modes *a*, Fig. 6-7). These are breathing of each Ta_4 basal plane associated with elongation along the associated pseudo-C_4 axis. The next band at 170 cm^{-1} is a full breathing of the Ta_6 cage with no Ta-Br^a motion (modes *b*, Fig. 6). The vibration mode associated forming the last intense band at 230 cm^{-1} is similar to the former with the additional shrinkage of the Ta_6 cage (mode *c*, Fig. 6-7). The less intense more energetic ones at 250 cm^{-1} are corresponding to three quasi-degenerated modes in which there is a tilt of alternatively each Ta_4 basal plane associated with the cooperative asymmetric stretch of the Br^i-Ta-Br^i units (modes *d*, Fig. 6-7). For the oxidized parent $[\{Ta_6Br^i_{12}\}Br^a_6]^{2-}$, the active vibrational modes are similar but noticeably shifted upon oxidation which lead to the lengthening of the Ta-Ta bonds and to the shortening of the Ta-Br^a ones: modes *a* from 115-120 cm^{-1} to 90-100 cm^{-1}; modes *b* at 170 cm^{-1} is found at 175 cm^{-1}; active mode *b'* at 135 cm^{-1}, similar to *b* but in which Ta-Br^a are involved in the breathing; mode *c* almost unchanged at 230 cm^{-1}; modes *d* shifted from 250 cm^{-1} to 245 cm^{-1}. The new mode *b'* is well separated from the other bands and can be an indication of the oxidation of the cluster unit.

In the absence of precise structural experimental data of $[\{Ta_6Br^i_{12}\}Br^a_2(H_2O)^a_4]$ geometry in $\mathbf{2}_{\alpha,\beta,\gamma}$, the optimized geometry of *trans*-$[\{Ta_6Br^i_{12}\}Br^a_2(H_2O)^a_4]$. $4H_2O$ was used as a model system since it better reproduces the Ta-Br^a elongation as previously shown (Fig. 5). Its simulated Raman spectrum is given in Fig. 6 and compared to the experimental $\mathbf{2}_{\beta[2]}$ Raman spectrum. The main bands already found for $[\{Ta_6Br^i_{12}\}Br^a_6]^{2-}$ and $[\{Ta_6Br^i_{12}\}Br^a_6]^{4-}$ are also present for this system (Fig. 6). An additional band labelled b_a is found at 155 cm^{-1}. It is highly similar to vibrational mode *b* to which bending motions of the Br^i-Ta-Br^i units in the basal plane are combined. A second additional band is found at 280 cm^{-1} and corresponds to the Ta-$(H_2O)^a$ stretching mode coupled with the rotation of one of the four crystallization solvent molecules (Fig. 6-7). It has to be emphasized that interactions existing in the solid-state structures between the water crystallization molecules and the neighboring clusters are not considered in the simulation. The intensity of this band so as the one of the mode *c* is thus altered by these non-constrained motions. Beside this artefact in the intensity of those two peaks, these results allow clearly to attribute the Raman bands in the 280-290 cm^{-1} region to presence of Ta-(H_2O)-containing cluster units in the samples.

The electronic excitations of $[\{Ta_6Br^i_{12}\}Br^a_6]^{n-}$ (n = 2-4) and $[\{Ta_6Br^i_{12}\}(H_2O)^a_6]^{2+}$ were computed by TD-DFT calculations to interpret the experimental UV-visible absorption properties of solutions of **1** in water and acetone (computational details in SI). The simulated spectra are given in Fig. 8 and the excitation energies and the nature of the main electronic excited states are detailed in Table S4. The calculated excitation spectrum of $[\{Ta_6Br^i_{12}\}Br^a_6]^{4-}$ (VEC=16) shows four main bands in the NIR-visible region.

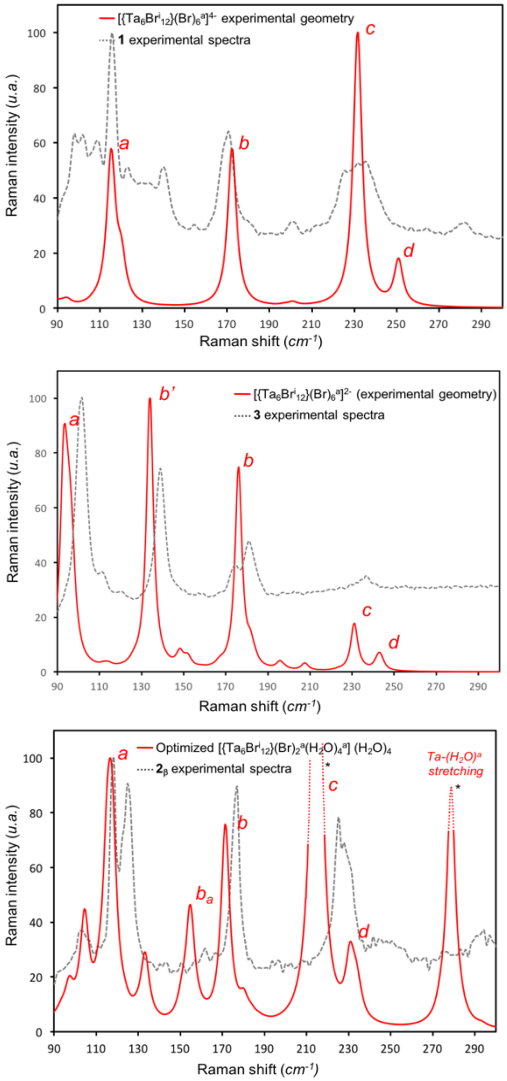

Fig. 6 Normalized simulated Raman spectra of $[\{Ta_6Br^i_{12}\}Br^a_6]^{4-}$, $[\{Ta_6Br^i_{12}\}Br^a_6]^{2-}$ and $[\{Ta_6Br^i_{12}\}Br^a_2(H_2O)^a_4].(H_2O)_4$ cluster units compared respectively to **1**, **3** and $\mathbf{2}_\beta$ powder experimental Raman spectra (dashed grey curves). *Vibration modes associated with rotational modes of the H_2O molecules bonded to the Br^a ligands via hydrogen bonds altering their intensities. Normalization of $[\{Ta_6Br^i_{12}\}Br^a_2(H_2O)^a_4].(H_2O)_4$ spectrum was thus performed using the *a* mode.

These bands **A**, **B**, **C**, **D** (given here in increasing energy ordering) are corresponding to electron excitations which descriptions are given in Scheme 2. **A** is described by an HOMO to LUMOs transition (MOs depicted in the right part of Scheme 2). These MOs are delocalized over the Ta_6 octahedron. The HOMO is globally metal-metal bonding in character whereas the three degenerated LUMOs (t_{1u} symmetry) are metal-metal antibonding. The bromine character of these MOs is much smaller (10 % and 31 % respectively). This excitation can be designated as Ta_6 to Ta^*_6 type (* = antibonding). The excitation giving rise to the band **B** can be described by a $(Ta_6\text{-}Br^a)^*$ to Ta^*_6 transition, whereas the band **C** which is more intense is Br^a to Ta^*_6 in nature. The band **D**, centered at 340 nm, corresponds to transitions between $(Ta_6\text{-}Br^a)^*$ to $(Ta\text{-}Br^a)^*$ orbitals (d/π^* to d/σ^*). The inner bromine ligands are involved in the excitations higher in energy (UV region).

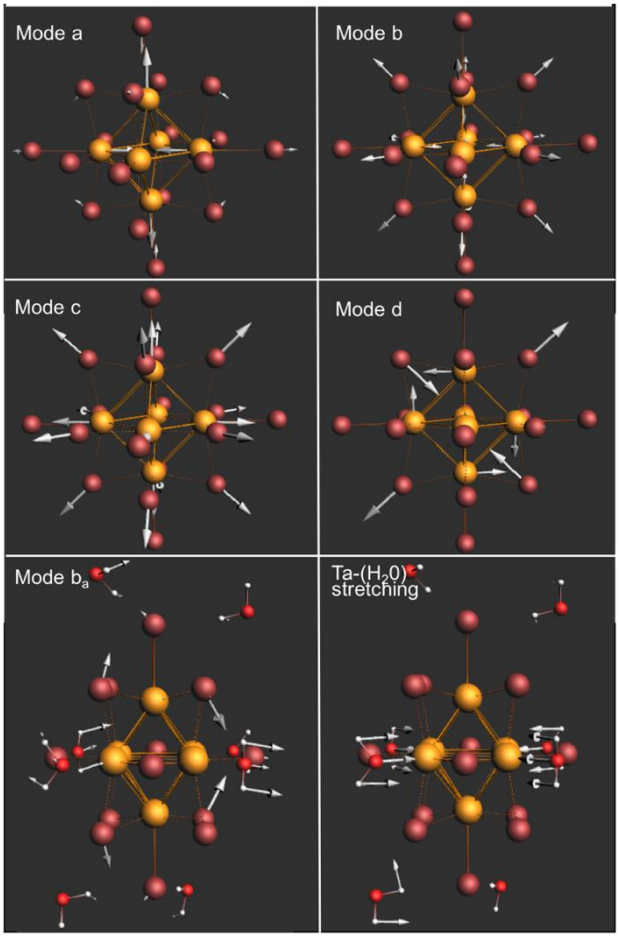

Fig. 7 Representation of the Raman active vibrational modes of $[\{Ta_6Br^i_{12}\}Br^a_6]^{4-}$ and $[\{Ta_6Br^i_{12}\}$*trans*-$Br^a_2(H_2O)^a_4](H_2O)_4$ indicated in Fig. 6.

The calculated excitation spectra of $[\{Ta_6Br^i_{12}\}Br^a_6]^{n-}$ upon successive oxidations from n = 4 to 2 reveals the appearance of low-energy excitations in the red-NIR region centered around 840 nm for n = 3 (VEC=15), and around 1230 nm for n = 2 (VEC=14). They are labelled **A'** and **N** respectively in Fig. 8. For n = 3, the low-lying band **A'** corresponds in fact to the band **A** observed for $[\{Ta_6Br^i_{12}\}Br^a_6]^{4-}$. This originates from the electronic and geometric reorganizations following the formal one-electron depopulation of the HOMO of $[\{Ta_6Br^i_{12}\}Br^a_6]^{4-}$ which induce a lowering of 0.38 eV lower of this band (Scheme 3). Upon two subsequent one-electron oxidations, the HOMO of $[\{Ta_6Br^i_{12}\}Br^a_6]^{4-}$ becomes vacant and becomes thus the LUMO of the $[\{Ta_6Br^i_{12}\}Br^a_6]^{2-}$ system. An **A** type transition cannot exist consequently anymore. The resulting MO energy diagram is shown in Scheme 3 in the Fermi region. The lower-lying allowed electronic transition for the two-electron oxidized compound, labelled **N**, occurs between the HOMO-5 and the new LUMO. It can be described as a $(Ta_6\text{-}Br^a)^*$ to Ta_6 transition. The presence of low-lying absorption bands is thus indicative of oxidation of the cluster unit (centered around 840 nm for VEC=15, and around 1230 nm VEC=14). The same trend is observed for other apical ligands since these excitations are mainly metal-centered (spin-)orbitals. Comparison with experimental UV-visible spectra of $\mathbf{1}_{acetone}$, $\mathbf{3}_{acetone}$, $\mathbf{3}_{DCM}$ in the red-NIR region (Fig. 4) is in agreement with the presence of $[\{Ta_6Br^i_{12}\}Br^a_6]^{2-}$ in solution. Even though the shift in nm of the maximum between experimental and computed values can appear large at first sight, it corresponds to only 0.25 eV of energy difference in that region of the spectra. This is an expected deviation at the level of theory employed. Additionally, the experimental data show that there is still a noticeable absorbance down to 1200 nm.

The experimental spectra of $\mathbf{1}_{water}$ and $\mathbf{2}_{\beta\text{-water}}$ (Fig. 4) can be reasonably compared to the simulated absorption properties of $[\{Ta_6Br^i_{12}\}(H_2O)^a_6]^{2+}$ units in water considering the mass spectrometry results. Nevertheless, we have estimated the first pKa of $[\{Ta_6Br_{12}\}(H_2O)_6]^{2+}$ to be 3.9 by titration of a solution of $\mathbf{2}_\beta$. We thus investigated the effect of deprotonation of $[\{Ta_6Br^i_{12}\}(H_2O)^a_6]^{2+}$ by simulating the absorption spectrum of $[\{Ta_6Br^i_{12}\}(H_2O)^a_5(OH)]^+$ and [*trans*-$\{Ta_6Br^i_{12}\}(OH)^a_2(H_2O)^a_4]^0$. The shortening of the Ta-O(H) distances (see Table 3) is associated with an elongation of the associated Ta(OH)-Ta bonds. This leads to a deviation from O_h symmetry and modifications in the MO energy diagrams (the HOMOs present an increased oxygen character (O(H)).

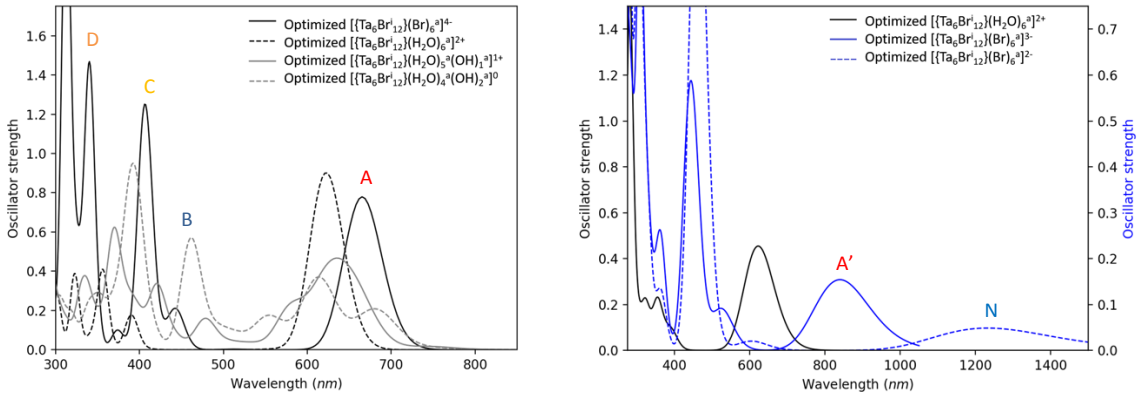

Fig. 8 Simulated absorption spectra of $[\{Ta_6Br^i_{12}\}Br^a_6]^{n-}$ (n = 2-4), $[\{Ta_6Br^i_{12}\}(H_2O)^a_6]^{2+}$, $[\{Ta_6Br^i_{12}\}(H_2O)^a_5(OH)_1]^{+}$ and $[\{Ta_6Br^i_{12}\}$*trans*-$(OH)_2(H_2O)^a_4]$.

The associated electronic excitations and simulated absorption spectra are thus presenting differences with the aqua-complex (Fig. 8). In the low-energy part of the absorption spectrum which is showing the greatest changes, it does induce a widening of the range of absorption around the position of the peak calculated for $[\{Ta_6Br^i_{12}\}(H_2O)^a_6]^{2+}$ at 622 nm and appearance of several maxima. Nevertheless, the double maxima observed experimentally is not fully explained and a dynamical treatment which would involve the hydrogen-bond network with the surrounding solvent water molecule and counterions would be necessary to better simulate the geometry changes (symmetry breaking). The deviations between experimental and computed absorption value ranges are of the order of 0.25 eV which is in line with benchmark studies at that level of theory. Nevertheless, the double maxima observed experimentally is not fully explained and a dynamical treatment which would involve the hydrogen-bond network with the surrounding solvent water molecule and counterions would be necessary to better simulate the geometry changes (symmetry breaking). The deviations between experimental and computed absorption value ranges are of the order of 0.25 eV which is in line with benchmark studies at that level of theory.

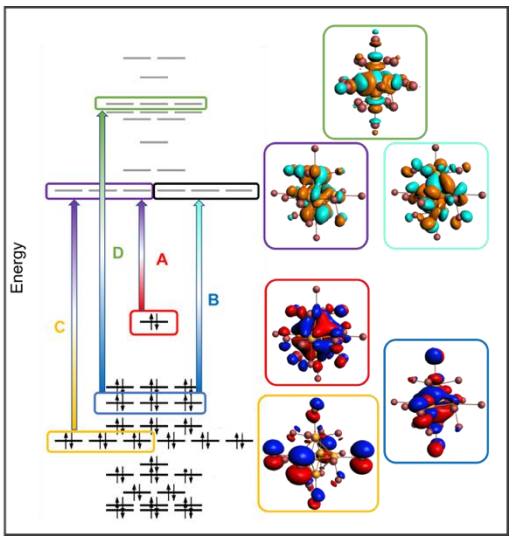

Scheme 2 Electronic transitions represented by colored arrows between MOs of $[\{Ta_6Br^i_{12}\}Br^a_6]^{4-}$. See Fig. 8 for the A, B, C and D labelling. MOs representation of the (iso-surfaces ± 0.02 e.bohr$^{-3/2}$; one of the symmetrically equivalent degenerated MOs is depicted for sake of clarity).

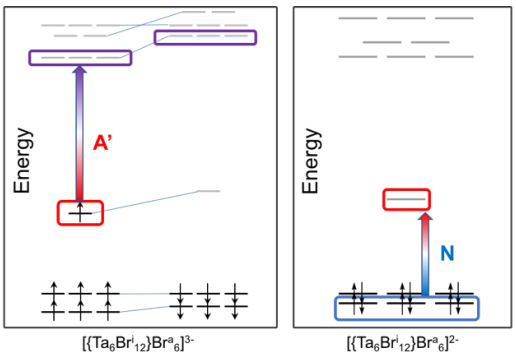

Scheme 3 Calculated electronic transitions between MOs (or spinorbitals) for $[\{Ta_6Br^i_{12}\}Br^a_6]^{3-}$ (left) and $[\{Ta_6Br^i_{12}\}Br^a_6]^{2-}$ (right) describing the nature of the bands A' and N respectively of the simulated absorption spectrum in Fig. 8.

Discussion

The solid-state compounds issued from aqueous solution of **1**, show that the $\{Ta_6Br^i_{12}\}$ cluster core, depending on the preparation methods, is coordinated to water molecules or combinations of (H_2O/OH), (Br/H_2O) or (Br/OH).[22, 29, 31-32, 45] The X-ray diffraction investigations combined with TGA have evidenced that the compounds $\mathbf{2}_\alpha$, $\mathbf{2}_\beta$ and $\mathbf{2}_\gamma$ are structurally related with solid-state structures derived from the one reported by Burbank *et al.* for $[\{Ta_6Cl^i_{12}\}Cl^a_2(H_2O)^a_4]\cdot 3H_2O$.[33] As demonstrated in this work, $\mathbf{2}_\alpha$, $\mathbf{2}_\beta$ and $\mathbf{2}_\gamma$ are all based on a $[\{Ta_6Br^i_{12}\}Br^a_2(H_2O)^a_4]$ cluster unit but they differ by their number of crystallization water molecules. These compounds show similar Raman spectra in the low-energy part (50-300 cm^{-1}, Fig. 1) as the fingerprint of the $[\{Ta_6Br^i_{12}\}Br^a_2(H_2O)^a_4]$ cluster building blocks. As revealed by the computational study, the chemical nature of the cluster unit, *i.e.* the apical ligands, and the oxidation state of $\{Ta_6Br^i_{12}\}$ modify the Raman response. The comparison between Raman theoretical and experimental results allows to first highlight that slight changes in the distances and deviations from O_h symmetry of the $[\{Ta_6Br^i_{12}\}Br^a_6]^{n-}$ unit alter the Raman signals (Fig. S11). Indeed, the simulated Raman spectra using the geometry $[\{Ta_6Br^i_{12}\}Br^a_6]^{2-}$ and $[\{Ta_6Br^i_{12}\}Br^a_6]^{4-}$ extracted from the available X-ray structures[17, 43] for the calculation which are of C_s and D_{3h} symmetry respectively lead to a much better agreement with the experimental spectra of **1** and **3** for the most intense peaks.

Concerning the structures of $\mathbf{2}_{\alpha,\beta,\gamma}$, we have been able to obtain a refined structural model only for $\mathbf{2}_\gamma$ (Fig. S2 and S3). It was determined by X-ray powder diffraction analysis using Rietveld methods starting with the Burbank model found for $Ta_6Cl_{14}\cdot 7H_2O$.[33] This model is based on an average orientation-disordered $[trans\text{-}\{Ta_6Br^i_{12}\}Br^a_2(H_2O)^a_4]$ cluster unit and on well-defined positions of the water crystallization molecules. In the computational study, this $[trans\text{-}\{Ta_6Br^i_{12}\}Br^a_2(H_2O)^a_4](H_2O)_4$ arrangement was used as starting optimized geometry. Indeed, by introducing explicitly the closest H_2O molecules around the $[trans\text{-}\{Ta_6Br^i_{12}\}Br^a_2(H_2O)^a_4]$ unit at the positions found in the Rietveld structural model of $\mathbf{2}_\gamma$, we have been able to mostly recover the weakening of the Ta-Br^a bonds. The water crystallization molecules enhance the signal involving Br^a owing to strong Br^a-(H_2O) interactions weakening the Ta-Br^a bonds. This strategy allowed to retrieve nicely the main features of the Raman experimental spectra of all the series of $\mathbf{2}_{\alpha,\beta,\gamma}$ compounds (Fig. 6). After this identification of the main peaks by comparison with the computational studies of $[\{Ta_6Br^i_{12}\}Br^a_6]^{2/4-}$ and $[trans\text{-}\{Ta_6Br^i_{12}\}Br^a_2(H_2O)^a_4]$ cluster units, it appears obvious that the surface of **1** solid-state powder samples contains, additionally to $[\{Ta_6Br^i_{12}\}Br^a_6]^{4-}$ cluster units, hydrated clusters (peaks at 102 cm^{-1}, and 278-290 cm^{-1} found in spectra of $\mathbf{2}_{\alpha,\beta,\gamma}$) and oxidized $[\{Ta_6Br^i_{12}\}Br^a_6]^{2-}$ units as well (peak at 104 cm^{-1} and peak at 139-140 cm^{-1} found in spectrum of **3**). These assumptions are fully corroborated by the computational results which undoubtedly attribute these peaks to vibrational frequencies specific of $[\{Ta_6Br^i_{12}\}Br^a_6]^{2-}$ and $[\{Ta_6Br^i_{12}\}Br^a_2(H_2O)^a_4]$. Actually, contrary to X-ray diffraction, Raman spectroscopy probes the surface of the crystallites where oxidation and hydrolysis and eventually water insertion obviously occur. We have indeed observed that **1** is sensitive to ageing in ambient air condition (moisture and O_2). The Raman spectra of **1** prepared using the same experimental protocol in slightly different atmospheric and ageing conditions show small differences in Raman spectroscopy (Fig. 1, batch 1 and 2). This is attributed to slightly different surface compositions (partial oxidation, hydrolysis and water insertion). The peaks around 100 cm^{-1} and 140 cm^{-1} are those which intensity is mostly altered. It indicates a difference in the proportions of oxidized clusters and of hydrolyzed ones between the two batches. This is in full agreement with the detection of peaks attributed to $[\{Ta_6Br^i_{12}\}Br^a_2(H_2O)^a_4]$ and $[\{Ta_6Br^i_{12}\}Br^a_6]^{2-}$ cluster units. An important finding of these Raman investigations is that presence of Raman peaks around 280 cm^{-1} are the signature of apical water molecules while a discrete peak around 140 cm^{-1} is characteristic of oxidized clusters (VEC =14).

X-ray powder diffraction pattern of **1** evidences $K_4[\{Ta_6Br^i_{12}\}Br^a_6]$ as major phase and KBr and Ta as byproducts. This feature added to the low quality of X-ray diffraction data renders difficult the accurate determination of the atomic coordinates from Rietveld refinement.

The combination of the mass spectrometry analyses, electrochemical properties, UV-visible absorption properties of solutions of **1**, $\mathbf{2}_\gamma$ and **3** allow to fully understand the different redox processes and chemical substitutions explaining the evolution of their

vibrational and absorption properties. Electrochemical studies of **3** in CH_2Cl_2 under normal conditions reveal the lowering of oxidation potentials of about 0.6 V compared to those measured in water. Beyond an expected negative shift in organic media compared with that observed in the aqueous medium is usual, this lowering is interpreted by the different nature of apical ligands. The cluster units in non-coordinating organic solvent are $[\{Ta_6Br^i_{12}\}Br^a_6]^{n-}$ while the stable cluster units in aqueous media are $[Ta_6Br^i_{12}(H_2O)^a_6]^{m+}$ and partially deprotonated ones depending on the pH. The analysis of mass spectra of acetone solutions of **1** allows to conclude that $[\{Ta_6Br^i_{12}\}Br^a_6]^{n-}$ cluster units are essentially present. Water containing clusters are also detected and are attributed to traces of H_2O in the solvent. The UV-visible absorption spectra of acetone solution of **1** shows a broad band centered at 930 nm which spread down to 1200 nm which is undoubtedly attributed to $[\{Ta_6Br^i_{12}\}Br^a_6]^{3-}$ oxidized cluster units on the basis of mass and electrochemical studies and quantum chemical simulations. Indeed, the electronic excitation calculations of $[\{Ta_6Br^i_{12}\}Br^a_6]^{2-}$, $[\{Ta_6Br^i_{12}\}Br^a_6]^{3-}$ and $[\{Ta_6Br^i_{12}\}Br^a_6]^{4-}$ are clearly different in the red-NIR absorption region. These low-energy excitations are of Ta_6 bonding to Ta_6 antibonding transition type. Interestingly, our calculations show that upon the substitution of bromine apical ligands by H_2O, the same band distinction is calculated in the NIR low-lying region upon VEC changes. The positions of the bands calculated for VEC = 14, 15 and 16 are in the same range of wavelengths that for the fully brominated systems of the same VEC. This reflects the fact that these excitations involve electronic density of Ta_6 core-centered and are thus less sensitive to ligand substitution. Indeed, mass spectrometry studies reveal that all apical bromine of the cluster $[\{Ta_6Br^i_{12}\}Br^a_6]^{4-}$ units are readily substituted in aqueous solution. $[\{Ta_6Br^i_{12}\}(H_2O)^a_6]^{n+}$ fragments are indeed characterized together with fragments having lost H^+ or H_2O groups. To sum up, the UV-visible absorption spectra in solution is a fingerprint of the oxidation state of the $\{Ta_6Br_{12}\}$-core since the electronic transitions in this part of the spectra are Ta_6-centered, the ligand being marginally involved. The presence of the low-lying bands which maxima are centered between 600 to 800 nm are indicative of a VEC = 16 of the $\{Ta_6Br_{12}\}$-core. On the other hand, red-NIR absorption bands (~900 - 1200 nm) are characteristic of oxidized clusters of VEC = 15 and/or 14.

Conclusion

This comprehensive step by step study of the behavior of $[\{Ta_6Br^i_{12}\}Br^a_6]^{4-}$] cluster unit in solution that results from the dissolution of $K_4[\{Ta_6Br^i_{12}\}Br^a_6$ reveals that it can undergo oxidation, ligand substitution and pH sensitivity. This changes noticeably modifies its physicochemical properties. $[\{Ta_6Br_{12}\}Br_6]^{4-}$ (VEC = 16) is highly negatively charged resulting in instability in solution. Indeed, it is easily oxidized by traces O_2 in organic solvent. The stable species in aprotic organic solvents are the fully oxidized $[\{Ta_6Br_{12}\}Br_6]^{2-}$ units (VEC = 14) affording distinctive red-brownish colored solutions. In water, a complete substitution of the bromine apical ligands of $[\{Ta_6Br_{12}\}Br_6]^{4-}$ by water molecules occurs. The resulting green emerald solution contains $[\{Ta_6Br_{12}\}(H_2O)_6]^{2+}$ (VEC = 16) which exhibits a poly-acidic behavior (first pKa ≈ 3.9).

The $\{Ta_6Br_{12}\}$ cluster core-based solid-state hydrates have been structurally characterized for the first time. They are built up from neutral [*trans*-$\{Ta_6Br^i_{12}\}Br^a_2(H_2O)^a_4$]. Short hydrogen bonds are formed between crystallization water molecules and the bromine apical ligands. It causes unusually long Ta-Br^a distances (2.80 Å av.) by stabilizing bromine ions and weakening consequently its interaction with the cluster core. The small modifications in the crystallization process of aqueous solutions lead to noticeable differences in the number of water molecules of crystallization and consequently in the packing and distances. We clearly show that Raman spectroscopy is the relevant technique to probe these subtle modifications.

In the context of using these clusters as functional building blocks with specific redox and optical properties to design functional materials,[14, 15] steps of solubilization are most of the time compulsory. This study constitutes an important contribution in the gain of knowledge about the exact nature of the molecular species when going from the solid-state to solutions and *vice-versa* allowing the optimization the protocols for the design of Ta_6 cluster-based materials.

Conflicts of interest

They are no conflicts to declare.

Acknowledgements

SIR (Rennes) Platform for Raman measurements (B. Lefeuvre). CDIFX (Rennes) T. Roisnel, V. Dorcet. K. C. acknowledges support by the French GENCI agency for HPC resources which were performed at the CINES and IDRIS (grant A0040800649, A0060800649). This work was partially supported by the Japanese Society for the Promotion of Science (JSPS) with the JSPS Fellowship of F.S. and JSPS KAKENHI (Grant No. JP18F18797). M.W. and C. L. acknowledge Saint-Gobain (SG), the National Institute for Materials Science (NIMS) and the Centre National de la Recherche Scientifique (CNRS) for their financial support. A part of this work was carried out in the France-Japan international collaboration framework ICGP NIMS-UR1.

References

1 A. W. Castleman and S. N. Khanna, *J. Phys. Chem.C*, 2009, **113**, 2664-2675.
2 V. K. Muravieva, Y. M. Gayfulin, C. Prestipino, P. Lemoine, M. R. Ryzhikov, V. V. Yanshole, S. Cordier and N. G. Naumov, *Chem. Eur. J.*, 2019, **25**, 15040-15045.
3 U. Schubert, *Chem. Mater.*, 2001, **13**, 3487-3494.
4 U. Schubert, *Chem. Soc. Rev.*, 2011, **40**, 575-582.
5 W. X. Zhang, P. Q. Liao, R. B. Lin, Y. S. Wei, M. H. Zeng and X. M. Chen, *Coord. Chem. Rev.s*, 2015, **293**, 263-278.
6 T. K. N. Nguyen, B. Dierre, F. Grasset, A. Renaud, S. Cordier, P. Lemoine, N. Ohashi and T. Uchikoshi, *J. Electrochem. Soc.*, 2017, **164**, D412-D418.
7 T. K. N. Nguyen, M. Dubernet, Y. Matsui, M. Wilmet, N. Shirahata, G. Rydzek, N. Dumait, M. Amela-Cortes, A. Renaud, S. Cordier, Y. Molard, F. Grasset and T. Uchikoshi, *Royal Soc. Open Sci.*, 2019, **6**, 181647.
8 M. Kepenekian, Y. Molard, K. Costuas, P. Lemoine, R. Gautier, A. G. Soraya, B. Fabre, P. Turban and S. Cordier, *Mater. Horiz.*, 2019, **6**, 1828-1833.
9 J. Lowe, D. Stock, R. Jap, P. Zwickl, W. Baumeister and R. Huber, *Science*, 1995, **268**, 533-539.
10 S. P. Christiano, J. L. Wang and T. J. Pinnavaia, *Inorg. Chem.*, 1985, **24**, 1222-1227.
11 S. Nagashima, S. Kamiguchi and T. Chihara, *Metals*, 2014, **4**, 235-313.
12 N. Prokopuk and D. F. Shriver, *Chem. Mater.*, 1998, **10**, 10-12.
13 M. A. Moussawi, N. Leclerc-Laronze, S. Floquet, P. A. Abramov, M. N. Sokolov, S. Cordier, A. Ponchel, E. Monflier, H. Bricout, D. Landy, M. Haouas, J. Marrot and E. Cadot, *J. Am. Chem. Soc.*, 2017, **139**, 12793-12803.
14 Renaud, M. Wilmet, T. G. Truong, M. Seze, P. Lemoine, N. Dumait, W. Chen, N. Saito, T. Ohsawa, T. Uchikoshi, N. Ohashi, S. Cordier and F. Grasset, *J. Mater. Chem. C*, 2017, **5**, 8160-8168.
15 T. K. N. Nguyen, A. Renaud, M. Wilmet, N. Dumait, S. Paofai, B. Dierre, W. Chen, N. Ohashi, S. Cordier, F. Grasset and T. Uchikoshi, *J. Mater. Chem. C*, 2017, **5**, 10477-10484.
16 W. Chen, M. Wilmet, T. G. Truong, N. Dumait, S. Cordier, Y. Matsui, T. Hara, T. Takei, N. Saito, T. K. N. Nguyen, T. Ohsawa, N. Ohashi, T. Uchikoshi and F. Grasset, *Heliyon*, 2018, **4**, e00654.
17 M. N. Sokolov, P. A. Abramov, M. A. Mikhailov, E. V. Peresypkina, A. V. Virovets and V. P. Fedin, *Z. Anorg. Allg. Chem.*, 2010, **636**, 1543-1548.
18 C. Chabrié, *C. R. Acad. Sci.*, 1907, **144**, 804-806.
19 W. H. Chapin, *J. Am. Chem. Soc.*, 1910, 32, 323-330.
20 P. A. Vaughan, J. H. Sturdivant and L. Pauling, *J. Am. Chem.Soc.*, 1950, **72**, 5477-5486.
21 R. D. Burbank, *Inorg. Chem.*, 1966, **5**, 1491-1498.
22 B. Spreckelmeyer, *Z. Anorg. Allg. Chem.*, 1968, **358**, 147-162.
23 H. Schäfer, B. Plautz and H. Plautz, *Z. Anorg. Allg. Chem.*, 1972, **392**, 10-22.
24 N. Brnicevic and H. Schäfer, *Z. Anorg. Allg. Chem.*, 1978, **441**, 219-229.
25 W. Koknat, J. A. Parsons and A. Vongvusharintra, *Inorg. Chem.*, 1974, **13**, 1699-1702.
26 B. G. Hughes, J. L. Meyer, P. B. Fleming and R. E. McCarley, *Inorg. Chem.*, 1970, **9**, 1343-1346.
27 M. Vojnovic, B. Peric, P. Planinic, G. Giester and N. Brnicevic, *Acta Cryst. C*, 2002, **58**, I71-I73.
28 B. G. Hughes, J. L. Meyer, P. B. Fleming and R. E. McCarley, *Inorg. Chem.*, 1970, **9**, 1343-1346.
29 B. Spreckelmeyer, *Z. Anorg. Allg. Chem.*, 1969, **365**, 225-242.
30 B. Spreckelmeyer, *Z. Anorg. Allg. Chem.*, 1969, **368**, 18-24.
31 B. Spreckelmeyer, C. Brendel, M. Dartmann and H. Schäfer, *Z. Anorg. Allg. Chem.*, 1971, **386**, 15-26.
32 B. Spreckelmeyer and H. G. von Schnering, *Z. Anorg. Allg. Chem.*, 1971, **386**, 27-37.
33 R. D. Burbank, *Inorg. Chem.*, 1966, **5**, 1491-1498.
34 R. D. Shannon, *Acta Cryst. A*, 1976, **32**, 751-767.
35 N. E. Cooke, T. Kuwana and J. Espenson, *Inorg. Chem.*, 1971, **10**, 1081-1083.
36 X. B. Xie and T. Hughbanks, *Inorg. Chem.*, 2000, **39**, 555-561.
37 N. T. K. Nguyen, A. Renaud, B. Dierre, B. Bouteille, M. Wilmet, M. Dubernet, N. Ohashi, F. Grasset, T. Uchikoshi, *Bull. Chem. Soc. Jap.*, 2018, **91**, 1763–1774
38 B. Spreckelmeyer and H. Schäfer, *J. Less-Common Met.*, 1967, **13**, 127-129.
39 F. Ogliaro, S. Cordier, J.-F. Halet, C. Perrin, J.-Y. Saillard and M. Sergent, *Inorg. Chem.*, 1998, **37**, 6199-6207.
40 E. Schott, X. Zarate and R. Arratia-Perez, *Polyhedron*, 2012, **36**, 127-132.
41 A. Kuc, T. Heine and T. Mineva, *Struct. Chem.*, 2012, **23**, 1357-1367.
42 P. Lemoine, J.-F. Halet and S. Cordier, *Struct. Bond.*, 2019, **180**, 143-190.
43 S. Cordier, C. Perrin and M. Sergent, *J. Solid State Chem.*, 1995, **118**, 274-279.
44 M. Wilmet, PhD Thesis, Université de Rennes 1, 2018.
45 B. Spreckelmeyer, *Z. Anorg. Allg. Chem.*, 1969, **368**, 18-24.